Continuous dynamic recrystallization in a Zn-Cu-Ti sheet subjected to bilinear tensile strain

M. Leonard[1,2,*], C. Moussa[3], A. Roatta[1,2], A. Seret[4], J. W. Signorelli[1,2]

[1] Instituto de Física Rosario (IFIR-CONICET/UNR), Ocampo y Esmeralda, Rosario (2000), Santa Fe, Argentina.

[2] Facultad de Cs. Exactas, Ingeniería y Agrimensura (FCEIA-UNR), Av. Pellegrini 250, (2000) Rosario, Argentina.

[3] MINES ParisTech, PSL - Research University, CEMEF, CNRS UMR 7635, CS 10207 1 rue Claude Daunesse, 06904 Sophia Antipolis Cedex, France.

[4] Technical University of Denmark, Department of Mechanical Engineering, Section of Manufacturing Engineering, 2800 Kgs. Lyngby, Denmark

*Corresponding author: leonard@ifir-conicet.gov.ar

Abstract

Research on zinc sheet formability, relevant for its technological applications, requires deeper understanding of the microstructural features that govern the plastic response of the material. In this work, a microstructural analysis by means of electron back-scattered diffraction (EBSD) technique was conducted on a commercial Zn-Cu-Ti sheet subjected to a bilinear tensile test at room temperature and low strain rate (5×10^{-4} s^{-1}). The refinement of the granular structure is analyzed in terms of the development of subgrains within initially large grains, which eventually evolve into high angle boundary grains. This continuous dynamic recrystallization (CDRX) mechanism appears as a key factor in order to explain the grain fragmentation process and the weakening of the texture observed during straining of this alloy.

Keywords: zinc sheet; continuous dynamic recrystallization; formability; texture.

1. Introduction

Zinc based alloys in the form of sheet have interesting applications in the architectural and building industry due to their good malleability and weldability, and their excellent corrosion resistance and surface aspect [1]. Early development of rolled zinc products included several alloys with small additions of copper, magnesium and/or aluminum to impart higher strength by means of solute strengthening or grain refining. The addition of titanium, in particular, remarkably enhances creep resistance to wrought zinc or Zn-Cu alloys, so the Zn-Cu-Ti alloy is now well established and it is the most widely used in sheet form for building applications such as facades, roofs or gutters [1,2].

Formability of zinc sheet is regularly good but it has some limitations. The most relevant drawback is the high anisotropy exhibited by the material due to the sharp crystallographic texture inherited from the rolling process. This strong texture is developed during deformation processing because of the reduced number of slip systems available in zinc, which has a hexagonal close-packed (HCP) crystal structure with c/a ratio of 1.856 [3]. Philippe et al. [4] and Fundenberger et al. [5] studied and simulated by means of the Taylor model [6] the texture evolution of several HCP materials, including a Zn-Cu-Ti alloy, relating the texture to the basic mechanical properties of the sheets (i.e., tensile strength and plastic anisotropy). Recent investigations dealing with experimental and modeling of zinc alloys formability have focused mostly on the anisotropic plastic behavior and its relationship with the forming limit strains. When a phenomenological approach has been used [7,8] the macroscopic behavior was captured by a Hill 90 yield criterion [9] in conjunction with a hardening power law which accounts for the temperature and strain-rate sensibility of the material. On a crystal plasticity approach, Schwindt et al. [10] improved the combination of the Marciniak-Kuczynski (MK) technique with the visco-plastic self-consistent (VPSC) model proposed originally by Signorelli et al. [11] to predict the forming limits of a Zn-Cu-Ti sheet with relatively good results. However, the model underestimates the forming limit curve (FLC) when the major strains are parallel to the rolling direction (RD). Cauvin et al. [12] also applied the VPSC model to analyze the mechanical anisotropy of a Zn-Cu-Ti alloy, focusing mainly on the tensile response and the texture evolution. Even though the crystal plasticity approaches are based on the deformation mechanisms operative at the grain scale, the works mentioned are based mostly on the texture evolution but not on topological aspects of the microstructure or dislocation-based hardening laws. Borodachenkova et al. [13] applied a microstructure-based hardening model embedded in the VPSC scheme to simulate texture evolution and mechanical response of a Zn sheet subjected to forward-reverse simple shear deformation. More recently, Schlosser et al. [14] experimentally analyzed the influence of bilinear strain paths (i.e., balanced biaxial expansion followed by uniaxial tension) on the formability of a Zn-Cu-Ti sheet. The extended, somewhat unexpected ductility encountered lead to the hypothesis that for an accurate modeling of zinc sheet formability it would be necessary to take into account not only texture but also the microstructure evolution in terms of grain fragmentation. In fact, microscopical evidence revealed a grain-refining process which cannot be entirely explained by slip activity and may be due to dynamic recrystallization [14].

Recrystallization processes which develop during deformation are generally categorized as dynamic recrystallization (DRX). These phenomena consist on the creation of new grains in the microstructure of a polycrystalline material subjected to plastic straining, reflecting a combination of thermally-activated and strain-induced mechanisms different from the typical static recrystallization process (SRX) which occurs during annealing. Depending on material properties and deformation conditions, DRX may take place as a discontinuous nucleation and growth process, which is known as discontinuous dynamic recrystallization (DDRX); or it may occur in a continuous fashion as a gradual creation of new grains, in which case it is termed continuous dynamic recrystallization (CDRX) [15,16]. Furthermore, it is possible that during straining a dynamic recovery process takes place (DRV), either as a preceding step to CDRX or preventing DDRX [16].

Mechanical response and microstructure evolution during warm or hot working of HCP materials are not as widely studied as in the case of cubic metals, especially regarding sheet forming. Most of the past and current literature deals with magnesium alloys, for which formability can be enhanced by DRX during warm/hot forming operations [17–19]. Mg and its alloys are known to undergo CDRX at low to intermediate temperature deformation through a mechanism of gradual lattice rotation near the original grain boundaries [20,21]. This mechanism is associated to plastic inhomogeneity due to the lack of sufficient slip systems in the low-symmetry, hexagonal crystal structure. Thanks to the advances in the electron back-scattered diffraction (EBSD) technique much research has been devoted during the last decades to understand the mechanisms responsible for CDRX in Mg alloys by means of orientation imaging microscopy (e.g., refs. [22–24]). Regarding zinc, it is extensively reported in the technical literature [1,2] that, owing to its low melting point (T_m = 693 K), recrystallization can occur at regular processing temperatures (room temperature corresponding to 293 K, i.e., ~0.42T_m). Little work hardening can be obtained for this reason, even for alloys containing solute additions which tend to elevate the recrystallization temperature [2]. However, only a few systematic studies can be found (most of them previous to the development of the EBSD technique) and the results concerning deformation mechanisms are not always concurrent. For instance, Neumeier and Risbeck [25] studied the creep behavior of Zn-Cu and Zn-Cu-Ti rolled slabs with varying composition and processing temperatures. They found a very fine-grained microstructure for the Ti-containing alloys rolled at room temperature and this was attributed to a non-conventional recrystallization mechanism. A Zn-0.4%Al alloy was found to exhibit room temperature superplasticity by Naziri and Pearce [26], a behavior which was explained by a combination of DRV and grain boundary sliding (GBS). Malin et al. [27] reported DRX in pure zinc rolled at room temperature up to moderately high strains. During the early stages of rolling, deformation was accommodated mostly by twin and slip, but at a strain of ~0.5 the deformation localized in shear bands consisting of recrystallized grains. With increasing strain, these DRX bands covered the whole volume of the samples, allowing further deformation by means of renewed slip and twinning activity. Solas et al. [28] developed an *N*-site VPSC model accounting for local interactions with the aim of simulating plastic deformation and recrystallization. The model was applied to commercial purity zinc (CP-Zn) deformed by channel-die compression at 398 K (~0.57T_m); at these conditions the material showed neither DRX nor twinning. Besides these rather divergent observations, most of the works mentioned focus mainly on the metallurgical aspects of the granular evolution of low-alloyed zinc and its relationship to the mechanical response, but not to their influence on anisotropy of the sheet products and their formability.

The aim of the present work is to investigate the microstructure evolution of a Zn-Cu-Ti sheet subjected to a bilinear tensile test by means of orientation imaging microscopy. The main features of this evolution are analyzed in terms of the grain size and morphology, as well as the development of substructures which account for a grain fragmentation process that shall be classified as CDRX. These results are complemented with an analysis of the orientation influence on the fragmentation behavior and a study on the boundary character of the subgrains, together with an evaluation of the effect of a higher strain rate.

2. Material and methods

The material chosen for this study is a commercial Zn-Cu-Ti sheet of 0.65 mm thick. The manufacturing process consists of continuous casting followed by rolling in two steps, the first one comprising two passes at high temperature. Then the sheet is coiled and the final rolling step consists on several passes near room temperature (~50–80 °C) until the final thickness is achieved. The chemical composition contains 0.094 Cu and 0.047 Ti (wt. %).

Orientation imaging analysis was carried out by the EBSD technique, using a Bruker Quantax EBSD system (comprising an e-Flash^{HR} detector and Esprit software) mounted on a Zeiss Supra40 field emission gun scanning electron microscope (FEG-SEM) operated at 20 keV. Maps having a size of 1200×900 data points were acquired over a square grid with a step of 94 nm (total map size: 122.8×84.6 μm). Post-processing of the EBSD data was done with the MTEX toolbox [29]. The misorientation angle to define a high-angle grain boundary was set as θ>12° (i.e., HABs). Boundaries with misorientation angles between 2° and 12° were considered as low-angle boundaries (LABs). Further details regarding the post-processing of the EBSD data are stated below. Pole figures for texture analysis were derived from the orientation distribution function (ODF) calculated from the raw EBSD data. This texture representation, for the size of the EBSD maps chosen, was found to be statistically reliable when compared to macroscopic textures measured on the as-received material by means of the X ray diffraction (XRD) technique. Moreover, the as-received texture shown below is in good agreement with the texture obtained by XRD for a different sheet of the same alloy [30]. The samples were mounted on a cold-setting epoxy resin, polished with SiC abrasive paper down to P2400 grit size (FEPA standard), then with 3 μm and 1 μm diamond suspension and finished with colloidal silica of ~0.05 μm average particle size.

The microstructure of the as-received Zn-Cu-Ti sheet revealed by EBSD is presented in Fig. 1, showing two band-contrast (BC) maps corresponding to the longitudinal (RD-ND) and in-plane (RD-TD) sections of the sheet (ND and TD refer to the normal and transverse directions with respect to the rolling direction, RD, respectively).

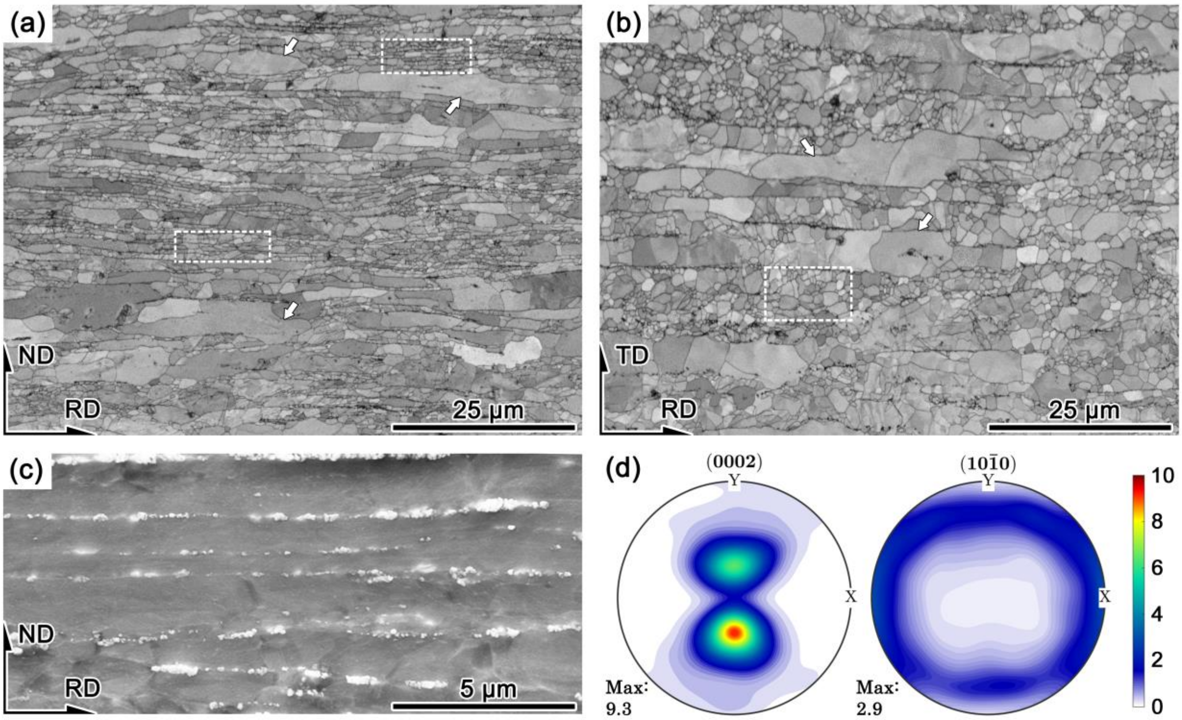

Figure 1. Microstructure and crystallographic texture of the Zn-Cu-Ti sheet in the as-received condition. (a) and (b): band contrast of the EBSD maps taken from the RD-ND and RD-TD sections, respectively. Some large, elongated grains are indicated by arrows and clusters of small, equiaxed grains are bounded in dashed boxes. (c) Secondary electron micrograph revealing the $TiZn_{16}$ phase. (d) Basal and prismatic pole figures recalculated from the EBSD data (X and Y labels correspond to TD and RD, respectively).

The morphology revealed by the BC maps presents a nearly bimodal distribution of grains, with a population of large, approximately pancaked grains, and a different population of smaller, more equiaxed grains (grain reconstruction is presented in section 3.2). Cu remains in solid solution for the composition reported [2]. The low solubility of Ti in Zn results in the formation of the intermetallic compound $TiZn_{16}$ [31], which is hardly seen in the BC maps because of the small size of their particles. These are shown in more detail in Fig. 1c by means of a secondary electron scan with higher magnification. The weight fraction of the intermetallic phase in the present alloy has been estimated at ~3% maximum [30]. It can be seen that the $TiZn_{16}$ particles are sub-micron sized and they form thin bands along the RD. This is the sheet microstructure inherited from the rolling process, which also results in the crystallographic texture shown by the basal (0002) and prismatic $\{10\bar{1}0\}$ pole figures in Fig. 1d. The main texture component consists of a majority of the grains having their *c*-axis pointing at ~23° of the normal direction in the ND-RD plane (the angle estimation has been done by calculating the orientations of the maxima of the ODF). It can also be seen that there is a subtle preferred orientation of the prismatic poles towards the TD. Such texture is typical for a rolled HCP aggregate with c/a>1.633, resultant of <a> basal slip ($(0001)\langle 11\bar{2}0\rangle$) accompanied by minor <c+a> gliding on the 2nd order pyramidal plane (i.e., $\{11\bar{2}2\}\langle 11\bar{2}3\rangle$ system) [3,4].

The analysis of the strain effect on the microstructure will be limited to uniaxial tensile (UAT) deformation along the RD in two steps. A non-standard sample (140×85 mm) was subjected to tensile loading along RD up to an early stage of localized necking, which corresponds to an average major true strain of ~0.35 (Fig. 2a). Then a smaller tensile sample (11×4 mm) was cut from a region which locally attained a prestrain of ~0.31, with its longitudinal axis also parallel to RD. The second test was conducted until fracture, giving a total accumulated major strain in the EBSD-analyzed zone of ~0.66. This two-step, bilinear tensile test (referred to as UAT+UAT) allowed for achieving higher deformation than with a regular tensile test, since the geometric effect of the diffuse neck is eliminated when cutting the smaller sample. Figure 2b shows the flow curves of the UAT+UAT test. It is worth noting that repeated tests gave similar results, with a maximum deviation in the second step of ~10% in flow stress and ~25% in total elongation (the relatively high spread in the latter is expected for this material [32].

All tests were carried out with an Instron 3382 universal testing machine at room temperature (~20 °C), applying a constant engineering strain rate of 5×10^{-4} s^{-1}. A second-step sample was deformed at 5×10^{-1} s^{-1} to test the effect of a high strain rate; the results are shown and discussed in Sec. 3.6. The large tensile sample was cut from the as-received sheet by a laser cutting machine; the smaller samples were extracted by means of electro-discharge machining (EDM). Both cutting processes were accomplished without significant heating of the material. The strains developed during the tests were determined by the digital image correlation (DIC) technique, as detailed in Schlosser et al. [14].

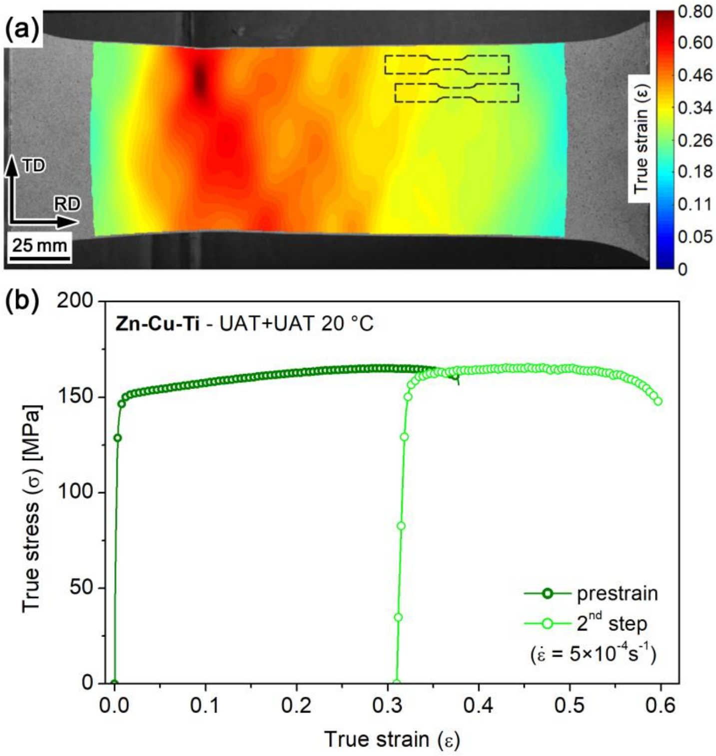

Figure 2. Bilinear tensile test (UAT+UAT) of the Zn-Cu-Ti sheet. (a) Sample pre-strained along RD with the major true strain field measured by digital image correlation. Geometry of the second UAT samples are shown in dashed lines. (b) Corresponding flow curves. The prestrain value of the second-step samples is ~0.31.

The EBSD scans for the deformed material were done over the RD-ND section of the samples, in a region between the middle plane of the sheet and the surface.

3. Results and discussion

3.1. Basic grain morphology and texture evolution

We take the BC data from the EBSD maps as a first approach to the grain morphology evolution (Fig. 3). It is apparent from these maps that the grain size tends to decrease with increasing strain level. Compared to the as-received condition (Fig. 1a), the UAT prestrain sample (Fig. 3a) seems to show fewer large grains. This trend is even more evident for the final stage of tensile loading (ε~0.66, Fig. 3b), in which there appears to be no grain with a size in the order of the initially large ones.

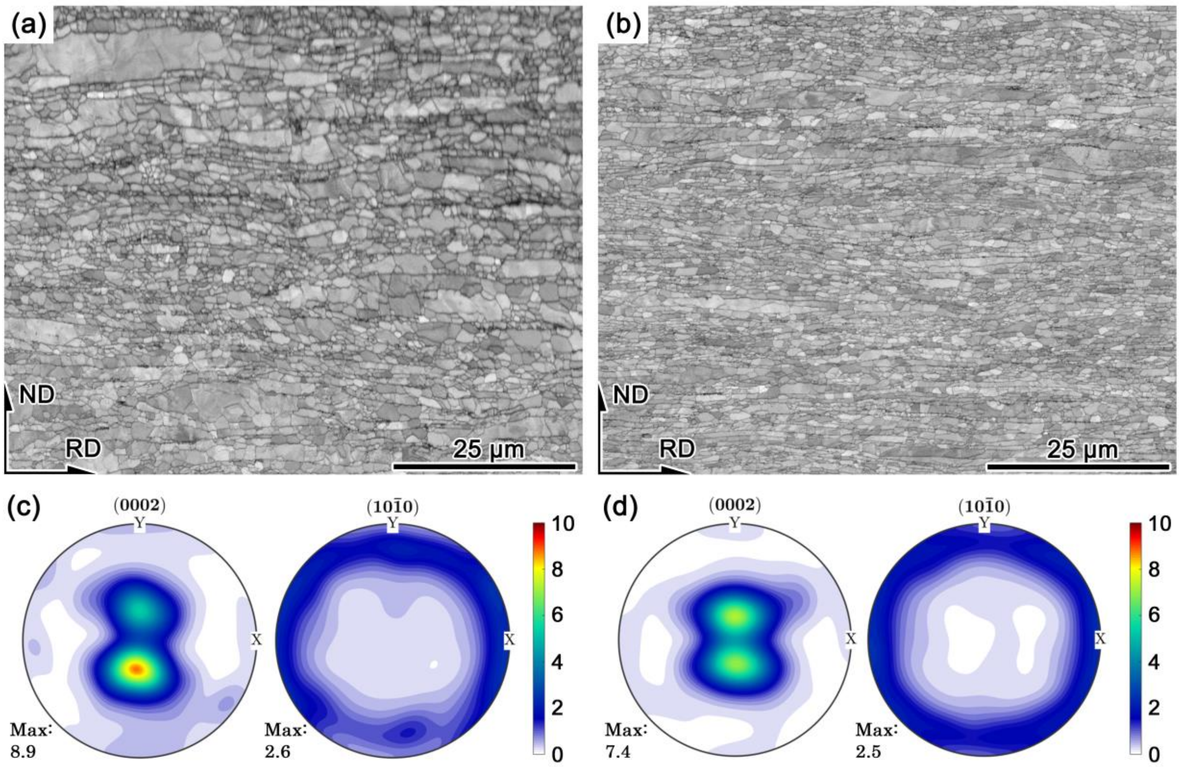

Figure 3. Band contrast maps and pole figures of the deformed Zn-Cu-Ti samples. (a) and (c): UAT prestrain (ε~0.31). (b) and (d): second UAT loading (ε~0.66). X and Y labels correspond to TD and RD, respectively.

Crystallographic texture of the deformed material, represented by the basal and prismatic pole figures (Figs. 3c and 3d), shows a modest decrease in intensity together with a rotation of the *c*-axis lying on the RD-ND plane towards the ND. The angular deviation between the maximum intensities and the ND changes from the initial 23° to 20° and 17° for the two successive tensile tests, respectively. The described evolution can be interpreted as a gradual rotation of the majority of the basal planes towards the plane of the sheet as a consequence of the basal slip activity, which is dominant in zinc [4,30]. However, the weakening of the main texture component should also be taken into consideration, as gliding alone on the basal system would not be enough to explain it. Moreover, there is a slight spread of the prismatic poles around ND at the end of the deformation process. The spreading of the main component and the rotation of the prismatic planes around ND can be related to CDRX, as it will be discussed below.

3.2. Grain size and shape evolution

Figure 4 shows the reconstructed grain boundaries from the EBSD data plotted over the inverse pole figure (IPF) maps. For reasons of visual clarity only a detail of each map is shown, representative of the sample as a whole. Black lines correspond to HABs (θ>12°) and gray lines to LABs (2°<θ≤12°). Only few twins can be seen in the microstructure. Considering zinc's compressive $\{10\bar{1}2\}\langle 10\bar{1}\bar{1}\rangle$ twinning system [33], twin boundaries were detected by the corresponding rotation angle and axis with a tolerance of 5° (ie., 86.03°$\langle 11\bar{2}0\rangle$ ±5°). This computation gave a total twin boundary density of 0.060, 0.059 and 0.049 μm/μm^2 for each strain level, which corresponds to only 4.5%, 4.1% and 2.5% of the total grain boundary density, respectively. A detail of the as-received IPF map is given in Fig. 4d in order to illustrate the detection of twin boundaries. Although twinning is usually a relevant deformation mechanism in HCP metals, the presence of Cu and Ti in zinc diminishes twinning activity, as observed by Philippe et al. [4] and Faur and Cosmeleată [34] for similar alloys.

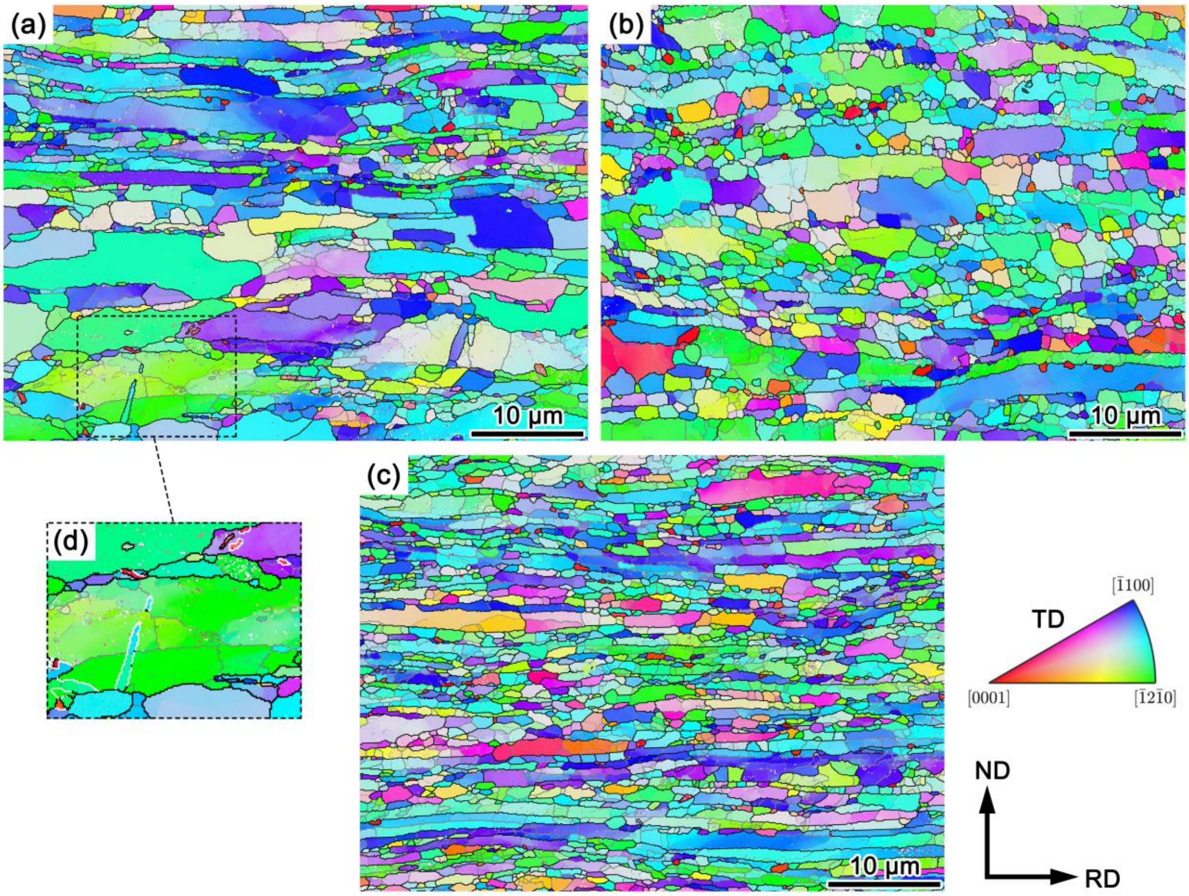

Figure 4. Grain boundaries plotted over orientation maps corresponding to the IPF with respect to the TD. (a) As-received; (b) UAT prestrain (ε~0.31); (c) second UAT loading (ε~0.66). Black lines: HABs (θ>12°); gray lines: LABs (2°<θ≤12°). (d) Detail showing $\{10\bar{1}2\}\langle 10\bar{1}\bar{1}\rangle$ twin boundaries in white.

Statistics derived from the grain reconstruction are shown in Fig. 5. Grain sizes are reported as an equivalent diameter value, which corresponds to the diameter of a disc having the same area of the polygonal shape of each reconstructed grain. This area-based approach allows to capture the shape effect when grains are not equiaxed, as in the present case. Grains with a diameter ≤0.33 μm (area ≤10 data points for the current step) were disregarded. For analysis purposes and taking into account the roughly bimodal distribution in the initial material, the set of grains in each sample was subdivided into two populations by a size criterion. All grains with an equivalent diameter greater than 3 μm were considered as large grains. The remainder grains belong to the set of small grains. Grain size and aspect ratio values reported in Fig. 5b and 5c correspond to the arithmetic mean of each population, while the error bars correspond to the standard deviation.

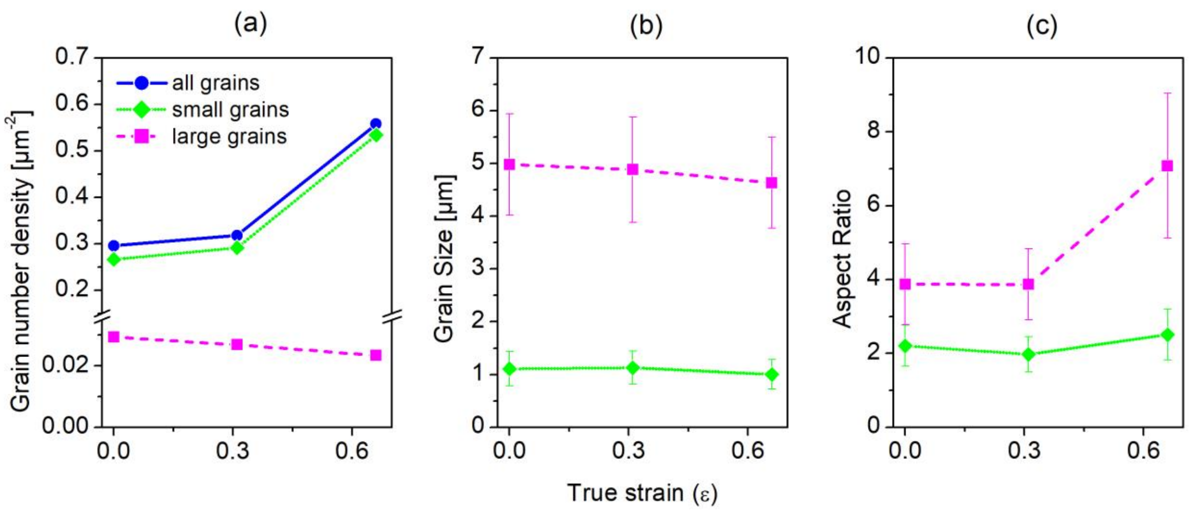

Figure 5. Grain statistics of the Zn-Cu-Ti sheet microstructure for each strain level, subdividing the populations by a size criterion: (a) number density of reconstructed grains; (b) average grain sizes (calculated as equivalent circle diameter); (c) mean aspect ratios. Error bars correspond to the standard deviation of each population.

As can be seen in Fig. 5a, the increase of strain correlates with an increase of the amount of grains in the microstructure. Most of this increase is due to the fragmentation of large grains leading to the multiplication of small grains. Indeed, the decrease in the number density of large grains (from 0.029 to 0.023 μm^{-2}, i.e., 25%) is accompanied by a slight reduction of their mean size (Fig. 5b). This double trend is related to the fact that the number increase of small grains accounts for a larger fraction of the map area: this fraction grows from 35% to 40% after the first UAT step, and up to 55% for the second test. It should be noted that the overall grain size of the specimens is relatively small, even for the grains considered large here. Particularly, for the set of smaller grains, their average value of ~1 μm is below the range of the typical grain sizes (~3–10 μm) achieved by means of standard thermomechanical processing [35]. Grain sizes of this order are reported in the early literature of fine-grained zinc sheets produced by rolling near room temperature [2,36]. Moreover, researchers seeking for superplasticity in Zn-0.4%Al alloy found an optimum grain size of approximately 0.5–1 μm without needing to apply severe plastic deformation processes [26,37].

Regarding the shape of the grains, from Fig. 5c it can be appreciated that the smaller grains are slightly elongated along the RD, but their aspect ratio stays almost constant throughout the whole deformation process. On the other hand, the remaining large grains –particularly at the highest UAT strain– are much more elongated along the RD. The stretching of grains along the direction of applied stress is typical for polycrystals accommodating plastic deformation; however, as it will be discussed below, in the case of the Zn-Cu-Ti sheet under study the elongation of the large grains is accompanied by their fragmentation.

3.3. Grain fragmentation by subgrain development

The LABs plotted on the maps of Fig. 4 allow visualizing the substructure development within the larger grains as a consequence of the imposed deformation. The formation of boundaries of low misorientation angles in the grain interiors is the typical microstructural feature of recovery or recrystallization occurring during deformation processing, i.e., DRV/DRX [15,16]. In the present case, observation of the microstructure reveals that the large grains suffer a subdivision or fragmentation process by developing LABs (either as closed subgrains or as inner boundaries which appears to be a transient step towards the formation of subgrains). A closer examination of this feature is presented in Fig. 6, in which a detail of the UAT prestrain map is shown.

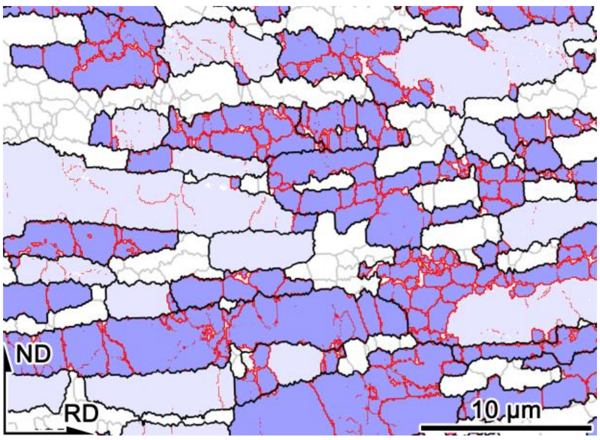

Figure 6. Map detail illustrating fragmentation of the larger grains (ε~0.31). Gray lines: HABs (θ>12°) of small grains (≤3 μm); black lines: HABs of larger grains (>3 μm); thick red lines: LABs (2<θ≤12°) of subgrains

within large grains; thin red lines: inner LABs. Blue: subgrains within large grains; light blue: large grains without subgrains or region of a large grain with an area greater than 50% of the whole grain area (i.e., unfragmented parent grains).

In order to analyze the general evolution of the subgrains with respect to their parent large grains, following Fig. 6 the subgrains or fragments are defined by the closed LABs ($2<\theta\leq12°$) within each large grain. A large grain is considered unfragmented if it does not have any subgrain or if it has an unfragmented area greater than the half of the total grain area. As Fig. 7 displays, there is an important increase of the number of subgrains during straining. Also, the fraction of unfragmented large grains tends to decrease markedly with deformation, meaning that within the bigger grains there is a relative increase in subgrain formation. This observation is clearly consistent with a fragmentation process. Moreover, the shape and the average size of the subgrains (thick red boundaries in Fig. 6) throughout the deformation course are equivalent to those of the small grains (gray boundaries in Fig. 6). In addition, the number density of subgrains and small grains increase in a similar way, as reported in Fig. 7.

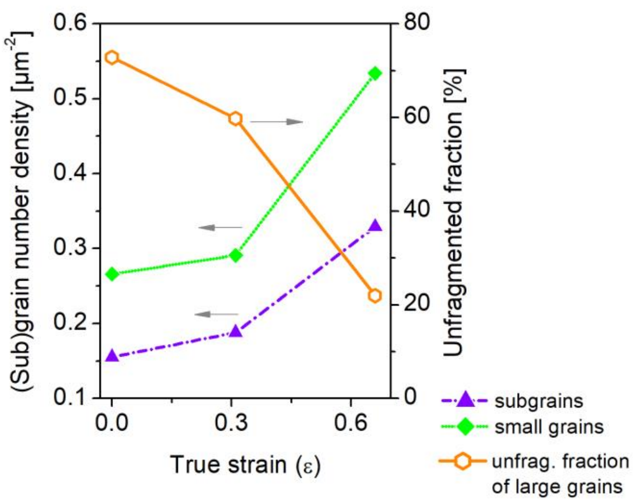

Figure 7. Evolution of the populations of grains and subgrains, and of the fraction of large grains which are not fragmented (number density of small grains is repeated from Fig. 5 for reference).

A closer inspection of the subgrains evolution can be realized by analyzing the misorientation gradient across the large grains, as shown in Fig. 8 where representative regions of the microstructure were selected. From the tensile prestrain (Fig. 8a) it is seen that many subgrains develop by progressive accumulation of misorientation from the center of the large parent grains to their boundaries, as displayed by the cumulative misorientation profiles over lines A1 and A2. The gradient over line A1 is smoother and the boundaries involved have low misorientation angles, reflecting an early stage of the fragmentation process for the selected grain. Subgrains crossed by line A2 have boundaries with higher misorientation and account for a more pronounced misorientation accumulation from the center of the parent grain to its boundary. This evolution is usually reported as the mechanism by which Mg alloys undergo CDRX due to progressive lattice rotation [20,23,38].

The misorientation profiles over lines B1 and B2 (Fig. 8b and 8e), corresponding to the highest strain level, reflect the evolved stage of the fragmentation process, since most of the boundaries between subgrains have higher misorientation angles than the preceding case. Moreover, some other boundaries have already surpassed the 12° threshold, thus becoming the HAB of a new small recrystallized grain. Note that most of the large grains in the map detail of Fig. 8b have become completely fragmented, as LABs have developed over their entire volume.

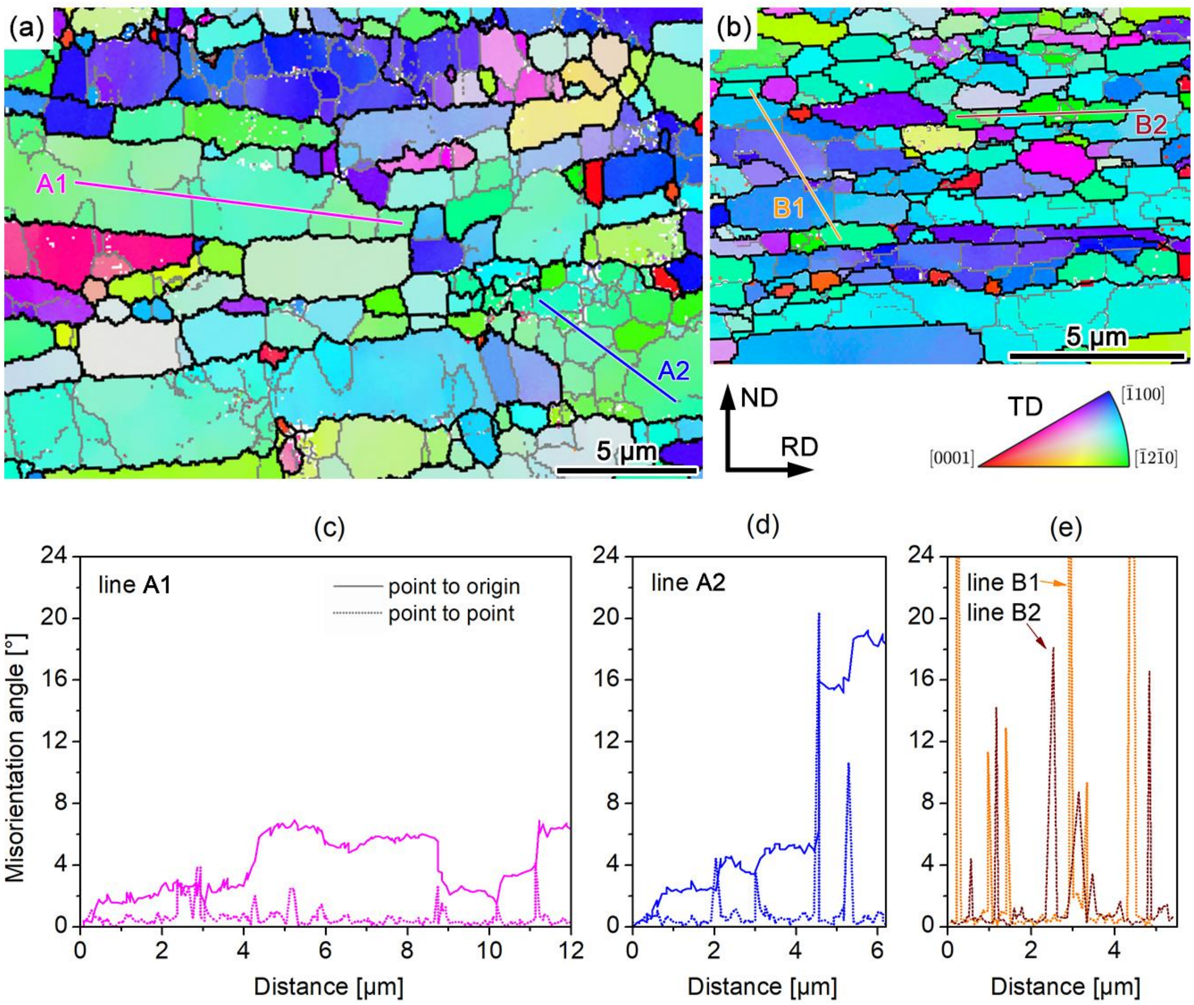

Figure 8. Misorientation gradients across fragmented grains: (a) and (b) EBSD map details of the first (ε~0.31) and the second (ε~0.66) UAT tests, respectively. (c–e) Changes of misorientation angle over the

lines indicated in the maps (solid lines: cumulative or point-to-origin misorientation; dotted lines: point-to-point misorientation).

In summary, the analyzed evolution of the (sub)boundaries and the similarities between the size and shape of the subgrains to those of the small grains, indicate a continuous fragmentation process which gives place to subgrains that evolve to become small grains with HABs. Similar observations have been reported for several Mg alloys which undergo CDRX at different deformation conditions [17,22,39,40]. Therefore, it is concluded that the grain refinement process observed during the deformation of the present Zn-Cu-Ti alloy can be classified as CDRX, with no significant influence of twinning.

Partitioning of the grain populations by size regarding their fragmentation behavior is consistent with an analysis of their internal orientation deviations. The average values of the orientation spread by grain –i.e., grain orientation spread (GOS)– is a typical parameter used for identifying recrystallized grains in deformed microstructures [24,41]. GOS maps for the studied conditions are displayed in Fig. 9a-c, while Fig. 9d shows the GOS value for the subpopulations of small and large grains, averaged over each map. It can be noticed that most of the small grains exhibit low GOS values and these keep almost constant during deformation. On the other hand, the large grains present a wider spread of GOS, although always higher in average than the small grains. Moreover, the average GOS for the set of large grains increases with strain. These values are compatible with the description of the large grains accommodating most of the strain by developing internal lattice distortions and subgrains, eventually leading to new, small recrystallized grains. Nevertheless, this analysis should not be taken as a definitive proof of CDRX due to the fact that the GOS parameter is sensitive to the grain size and shape [41,42]; this is the reason why the former subgrain analysis is preferred.

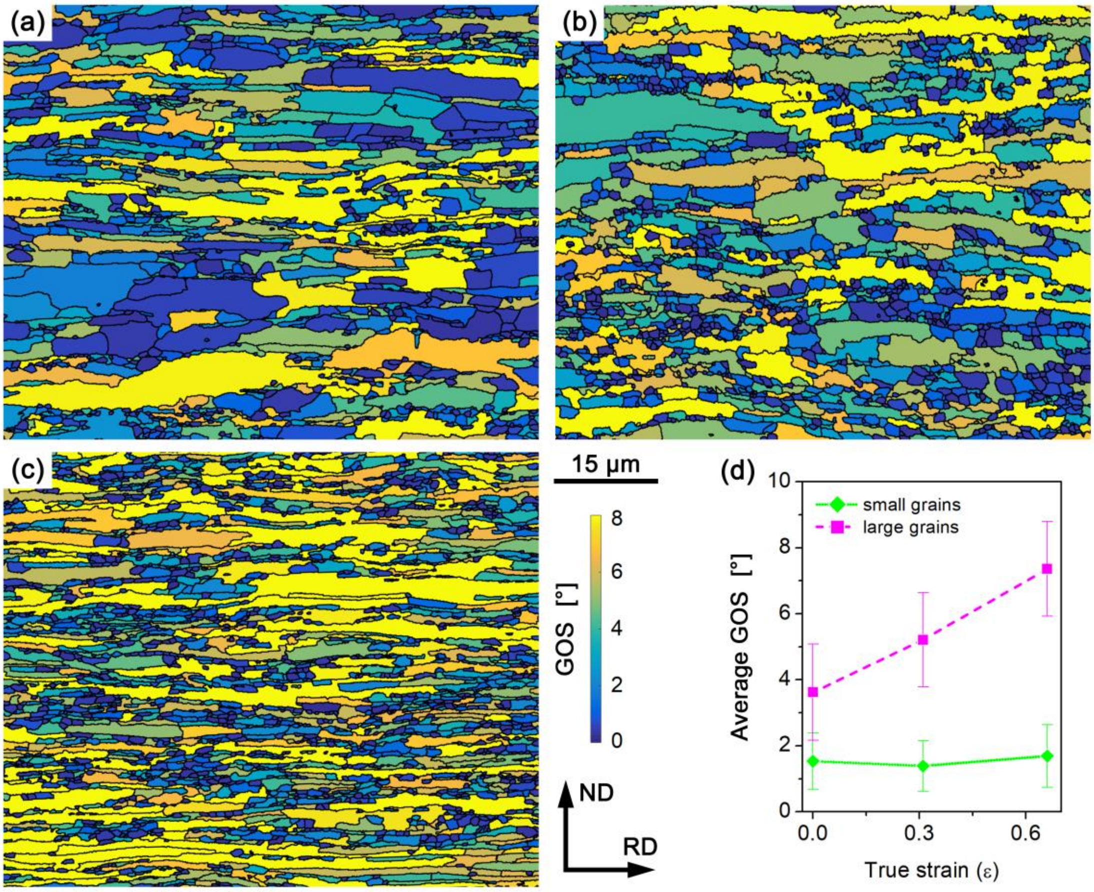

Figure 9. Grain orientation spread (GOS) maps for the Zn-Cu-Ti sheet under study. (a) As-received; (b) UAT prestrain (ε~0.31); (c) second UAT loading (ε~0.66). HABs (θ>12°) are displayed in black lines. (d) Average GOS values for the subpopulations of grains in each map (error bars correspond to the standard deviation).

It is interesting to note that the fragmentation process described so far does not appear to start with the tensile straining, as the initial microstructure already reveals an important amount of subgrains and internal LABs within the large grains. Evidently, the previous warm-temperature rolling process of the sheet produces a partial fragmentation of the cast and hot-rolled structure in a way that can be inferred from the EBSD data of the as-received material. Additionally, although the present study is not intended to investigate the manufacturing process of the commercial sheet, the presence of the $TiZn_{16}$ phase particles along some of the grain boundaries (Fig. 1c) may contribute to the fragmentation mechanism described. Early studies on low-alloyed zinc attributed the grain-refining ability of the Ti-bearing alloys to the intermetallic particles [25]; and it was also reported that impurity particles along grain boundaries in rolled CP-Zn stabilize its fine-grained structure [36].

3.4. Influence of orientation on the fragmentation behavior

Concerning the orientations of the large grains and their relationship with the main texture component, the fragmentation behavior appears to be different between the grains which have their *c*-axis pointing away from the ND and those whose basal planes are more closely parallel to the plane of the sheet. In this regard, we split the population of large grains into two groups according to their average orientation: (I) the large grains with their *c*-axis having an angular deviation to the ND greater than 45°, on one hand; and (II) those large grains whose basal planes are inclined to the plane of the sheet closely than 45°, on the other. The grains which fulfill the first condition for the three states considered represent a fraction of only 20%, 18% and 11%, respectively, of the total population of large grains. Meanwhile, group II involves the large grains that are part of the main texture component. Following Fig. 10a, the fragmented fraction of the large grains belonging to group I is smaller than the one of group II, particularly in the initial state. After the first tensile test there is a marked increase in the fragmented portion, but this is still smaller than the fraction of grains which develop subgrains near the main texture component (group II). Moreover, the average number of subgrains contained in the fragmented grains (Fig. 10b) is higher for group II; and this value increases with strain more rapidly than the amount of subgrains within group I. Average grain sizes of both groups are almost the same. In summary, the grains oriented near the main texture component are more easily fragmented than the ones which have their *c*-axis pointing away from the plane of the sheet, accounting for ~90% of the subgrains developed along the whole deformation process.

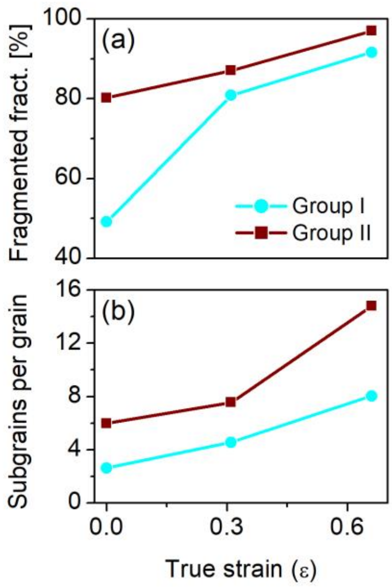

Figure 10. Differences in the fragmentation process of the Zn-Cu-Ti sheet according to the mean orientation of the larger grains. Group I: large grains whose *c*-axis have an angular deviation to the ND greater than 45°; group II: large grains with *c*-axis inclined to the ND closely than 45°. The fragmented fraction (a) and the average amount of subgrains per grain (b) are higher for grains of group II.

Differences in grain fragmentation behavior according to orientation are common in other materials, such as in FCC metals having grains with the Goss orientation [15]. In the case of hexagonal alloys, due to their anisotropy it is expected that preferred orientation plays even a major role in the DRX mechanisms, and that is the case in fact for Mg alloys, as reviewed by Kaibyshev [18]. Del Valle and Ruano [43] found that DRX is enhanced in an AZ31 alloy subjected to tensile straining at ~0.5–0.6T_m when the stress axis is normal to the *c*-axis in samples with a strong basal fiber. They attributed this behavior to the enhancement of multiple-slip instead of basal single-slip. Likewise, Kaibyshev [18] states that, since non-basal glide is mandatory for the development of CDRX in Mg alloys, textures which hinder basal activity are optimal for grain-refining by means of CDRX. Thus, these observations are similar to the current Zn-Cu-Ti sheet in the sense that the CDRX process is enhanced for the grains having their *c*-axis more close to the ND, in which basal slip is geometrically less favored than <c+a> 2nd order pyramidal glide. Furthermore, simulations by means of the affine-VPSC model (assuming relative critical shear stresses of 15 and 10 for the prismatic and the 2nd order pyramidal systems, respectively, with respect to the basal system; and an aspect ratio of the ellipsoidal inclusion of 2.4:1.4:1, which corresponds to the average aspect ratio of the as received microstructure) show that grains belonging to group II present ~60% more pyramidal <c+a> activity than grains in group I.

3.5. Boundary analysis

Regarding the fragmentation process of the grains in group II, the evolution of their subgrains' boundaries can be further analyzed in terms of their angles and axes of misorientations. By counting the length of the LABs with a misorientation angle range of $2°<\theta\leq6°$ and $6°<\theta\leq12°$, we can estimate the fraction of these kind of boundaries for the three levels of strain. This counting includes the inner LABs which do not form a closed subgrain, in order to capture the gradual process of formation of a fragment. It is important to note that these inner boundaries account for almost half of the fraction of LABs in the initial state. Although the fraction of $2°<\theta\leq6°$ approximately doubles the $6°<\theta\leq12°$ portion for the three strain levels, the former fraction decreases with strain (from ~19% to ~16%) and the latter increases from ~8% to ~11%. Also, the inner LABs which still do not form a subgrain belong mostly to the 2°<θ≤6° range and their total length reduces notably between the as-received and the final condition.

Figure 11 shows the distribution of misorientation axes of the LABs, separated into the two angular ranges previously mentioned; and also of the boundaries between small grains having a misorientation angle 12°<θ≤20° –i.e., those subgrains which we assume that have evolved from LABs to HABs. The axes distributions are shown in Fig. 11 as probability density plots in the unit triangle of the stereographic projection, reflecting the relative importance of certain axes of misorientation across boundaries. The 2°<θ≤6° fraction of LABs presents axes distributions predominantly based on rotations around directions lying on the basal planes (<*hki*0> directions), particularly for the lower levels of deformation. On the other hand, for the LABs in the range of 6°<θ≤12°, the axes distributions show an increasing tendency of rotations around the basal plane's normal. Moreover, it is interesting to note that the boundaries between the newly formed small grains have also an axis distribution concentrated in the basal pole, even more pronounced than the former LABs.

Applying the same analysis to the LABs developed within the large grains oriented away from the plane of the sheet (group I), it was found that the axis distribution corresponds mostly to rotations around the <*hki0*> directions. This tendency is the same for the whole range of LABs.

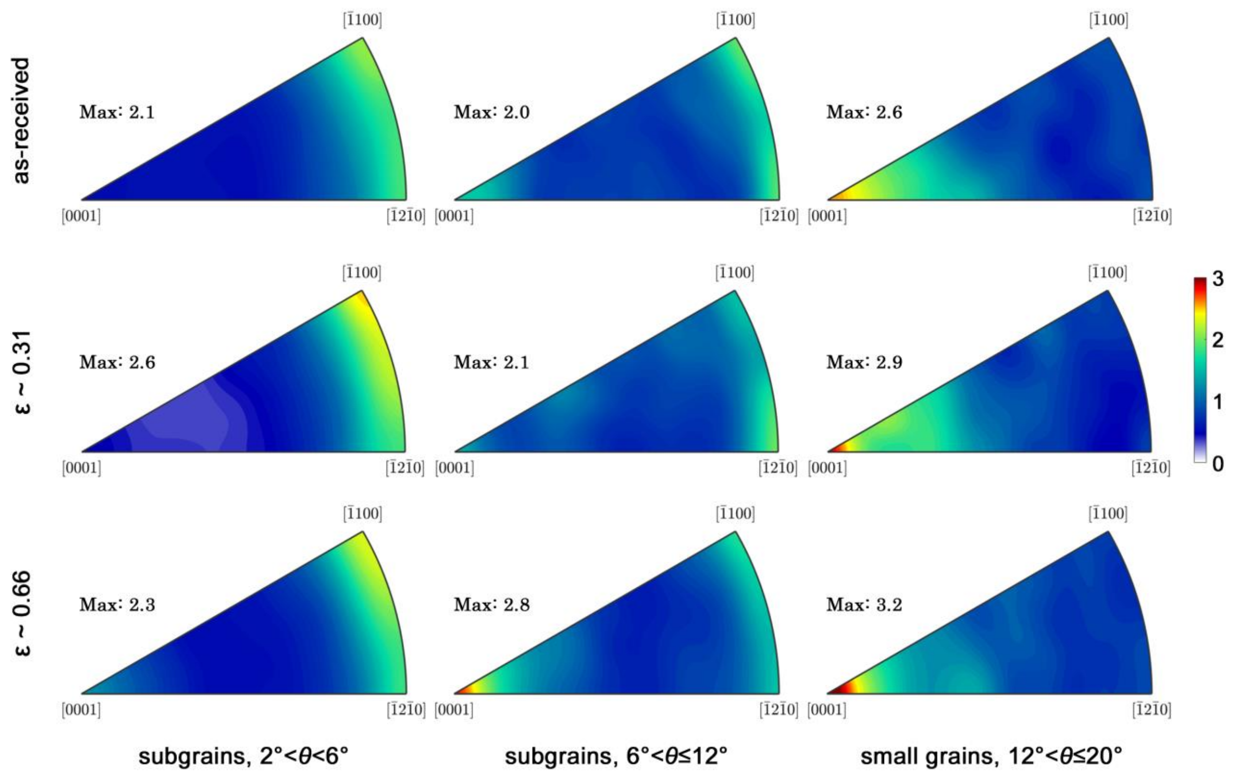

Figure 11. Distribution of misorientation axes across boundaries (within the group of grains with c-axis deviation from the ND <45°) for the conditions indicated. Left and middle columns: LABs within large grains in the angular ranges specified. Right column: HABs of small grains with misorientation angles ranging from 12° to 20°.

From a crystal plasticity point of view, differences of orientation between (sub)grains by rotations around an axis parallel to the basal plane would be explained by slip in the basal <a> or pyramidal <c+a> systems. Rotations about the *c*-axis, on the other hand, could be due to prismatic <a> slip by a Taylor-axis analysis [24] or by multiple glide of the pyramidal <c+a> systems. Since prismatic <a> activity is rarely found in Zn at room temperature [44,45], the rotations around the *c*-axis observed for the intermediate misorientation ranges (i.e., between 6° and 20°) could be attributed to multiple slip of 2nd order pyramidal system. This is consistent with the above discussion about the role of <c+a> activity in CDRX for the grains in group II.

Even though this analysis would require a more thorough examination of the boundary character and the local geometrically-necessary dislocations, the mechanisms involved can explain the stability and the moderate weakening of the crystallographic texture observed during straining. Indeed, the grains originally inclined away from the sheet plane tend to rotate –mainly by basal slip– toward the ND, stabilizing the principal texture component. Meanwhile, the large grains oriented near the main texture component accommodate deformation mostly by developing subgrains which have similar orientations to that of their parent grains, though with moderate rotations around both the <*hki*0> directions and the *c*-axis due to a combined activity of basal <a> and pyramidal <c+a> dislocations. These rotations make up the slight dispersion of the texture around its main component. Similar findings regarding texture weakening by subgrain rotation during CDRX have been reported in the literature on Mg alloys [39,40].

3.6. Effect of a higher strain rate

Since CDRX is a strain and thermally activated phenomenon [15,21], and considering that for Zn room temperature corresponds to $0.42T_m$, it would be expected that a change in strain rate may influence the deformation mechanisms in the material under study. In this regard, a tensile test of a second-step sample was carried out at a strain rate of 5×10^{-1} s^{-1} (i.e., three orders of magnitude faster than the previous tests) and the obtained microstructure was analyzed. The corresponding flow curve and EBSD map are included in Fig. 12.

Tensile response at this high strain rate (Fig. 12a) exhibits ~73% higher maximum true stress and ~33% lower total engineering elongation, reflecting the relatively high strain-rate sensitivity of this alloy. Also, the shape of the flow curve shows that at higher strain rate the work-hardening effect is increased. The differences briefly outlined may reflect the changes noticeable in the microstructure. In fact, the EBSD map (Fig. 12b) reveals more twins and larger grains for this microstructure when compared to the corresponding low strain-rate map (Fig. 4c). Twin boundary density is 0.209 μm/μm^2, approximately 4.2 times higher than the value for the slow strain rate test. Applying the same fragmentation criterion described above, as shown in Fig. 12c, after the present test there is a 48% of remaining parent large grains, implying an important difference with respect to the 23% corresponding to the slow tensile test. Also, the amount of subgrains and small grains is considerably smaller, so it is evident that the fragmentation mechanism is not as easily operative at this higher strain rate.

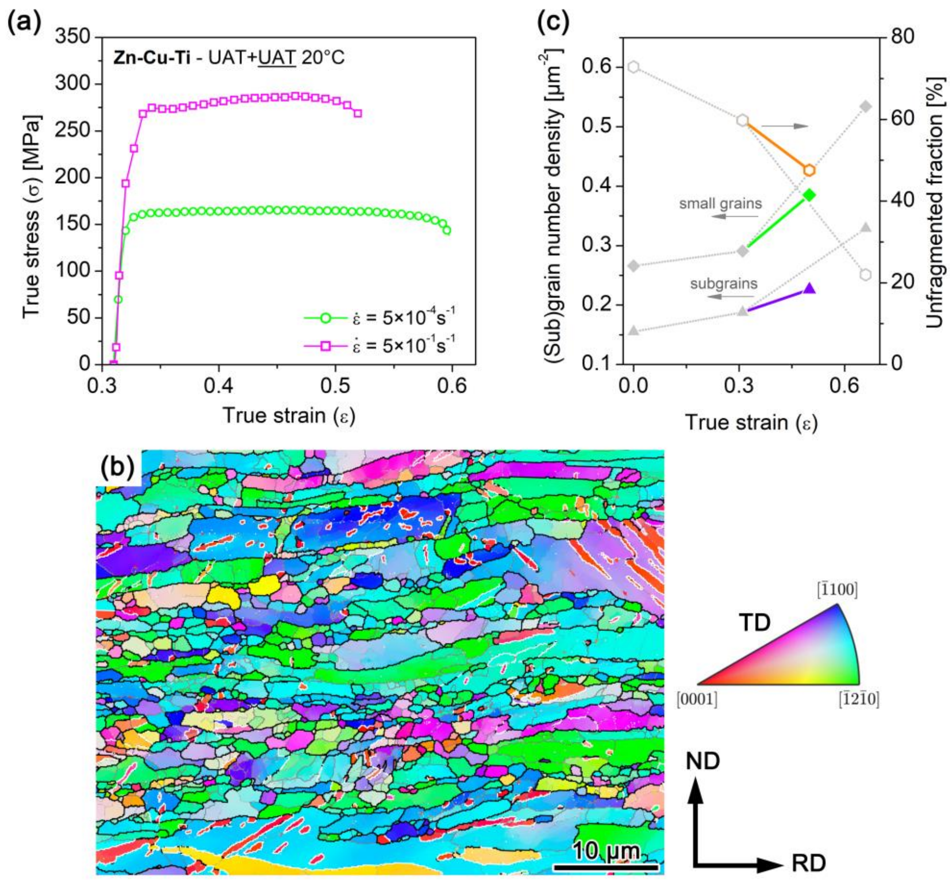

Figure 12. Effect of a higher strain rate (5×10^{-1} s^{-1}) on the second UAT test of the Zn-Cu-Ti sheet. (a) Flow curve (the second low-strain rate test is repeated for reference). (b) EBSD map for the high strain-rate test (total strain level ~0.50): grain boundaries plotted over IPF-TD map; black lines: HABs (θ>12°), gray lines: LABs (2°<θ≤12°), white lines: $\{10\bar{1}2\}\langle 10\bar{1}\bar{1}\rangle$ twin boundaries. (c) Comparison of (sub)grain numbers and

fragmented fractions of large grains between low (gray dotted lines) and high strain rates (colored solid lines).

It seems clear now that, for the lower strain rate, CDRX is a non-negligible deformation mechanism which allows the microstructure to accommodate macroscopic strain by formation and rotation of subgrains and of the newly developed small grains. However, since CDRX is a thermally activated process, if the strain rate is increased at the amount applied, there is not enough time for the microstructure to develop profuse CDRX and slip is no longer sufficient for accommodating the imposed deformation. Twinning is evidently activated at these conditions, but it is not enough for strain accommodation so the macroscopic failure is achieved at a lower strain level.

Additionally, from the preceding observations, it can be inferred that the extended ductility found by Schlosser et al. [14] during bilinear strain paths of the current Zn-Cu-Ti alloy at the same conditions (i.e., room temperature and strain rate of 5×10^{-4} s^{-1}) may be explained by the CDRX process, since a similar grain fragmentation behavior was observed in the corresponding microstructures, as it was preliminarily shown in that work.

4. Conclusions

The analyzed Zn-Cu-Ti sheet subjected to tensile straining at room temperature and slow strain rate shows a grain fragmentation process which can be categorized as continuous dynamic recrystallization. This process exhibits a growing development of subgrains of low misorientation (LABs) within initially large grains, which gradually increase their number and become new grains by the continuous increase of their misorientation.

The texture evolution reflects the combination of plastic slip with CDRX, since the *c*-axes tend to keep around the main texture component but with increasing deviation towards the ND and slight rotations of the prismatic poles due to the subgrain development. Furthermore, the grain fragmentation process due to CDRX is orientation dependent, since the large grains which belong to the main texture component exhibit more abundant subgrain formation.

The misorientation analysis applied to the LABs and to the low-angle fraction of small grains suggests that CDRX may be associated with enhanced activity of 2nd order pyramidal <c+a> slip. Increasing the strain rate results in a noticeable change of the deformation mechanisms, as the microstructure develops twinning in detriment of CDRX. This in turn is related to an important raise of the flow stress and a loss of ductility.

Acknowledgements

The authors would like to acknowledge Suzanne Jacomet and Cyrille Collin for their important help on sample preparation and EBSD scans. We are also grateful to Nathalie Bozzollo for fruitful discussions about the experimental results. The research leading to this work was partially funded by the Ecos Sud–MINCyT A16E03 project and PICT-A 2017-2970 grant.

Data availability

The raw/processed data required to reproduce these findings cannot be shared at this time as the data also forms part of an ongoing study.

References

[1] F. Porter, Zinc Handbook: Properties, Processing and Use in Design Mechanical Engineering, 1st ed., Marcel Dekker, Inc., New York, 1991.

[2] P. Chollet, Recent progress in the metallurgy of wrought-zinc alloys, Can. Metall. Q. 7 (1968) 177–185. https://doi.org/10.1179/cmq.1968.7.3.177.

[3] Y.N. Wang, J.C. Huang, Texture analysis in hexagonal materials, Mater. Chem. Phys. 81 (2003) 11–26. https://doi.org/10.1016/S0254-0584(03)00168-8.

[4] M.J. Philippe, F. Wagner, F.E. Mellab, C. Esling, J. Wegria, Modelling of texture evolution for materials of hexagonal symmetry–I. Application to Zn alloys, Acta Metall. Mater. 42 (1994) 239–250.

[5] J.J. Fundenberger, M.J. Philippe, F. Wagner, C. Esling, Modelling and prediction of mechanical properties for materials with hexagonal symmetry (Zn, Ti and Zr alloys), Acta Mater. 45 (1997) 4041–4055. https://doi.org/10.1016/S1359-6454(97)00099-2.

[6] G.I. Taylor, Plastic Strain in Metals, J. Inst. Met. 62 (1938) 307–324.

[7] Y. Jansen, R.E. Logé, M. Milesi, E. Massoni, An anisotropic stress based criterion to predict the formability and the fracture mechanism of textured zinc sheets, J. Mater. Process. Technol. 213 (2013) 851–855. https://doi.org/10.1016/j.jmatprotec.2012.12.006.

[8] M. Milesi, R.E. Logé, Y. Jansen, Anisotropic mechanical behavior and formability criterion for zinc sheets, J. Mater. Process. Technol. 214 (2014) 2869–2876. https://doi.org/10.1016/j.jmatprotec.2014.06.023.

[9] R. Hill, Constitutive modelling of orthotropic plasticity in sheet metals, J. Mech. Phys. Solids. 38 (1990) 405–417. https://doi.org/10.1016/0022-5096(90)90006-P.

[10] C. Schwindt, F. Schlosser, M.A. Bertinetti, M. Stout, J.W. Signorelli, Experimental and Visco-Plastic Self-Consistent evaluation of forming limit diagrams for anisotropic sheet metals: An efficient and robust implementation of the M-K model, Int. J. Plast. 73 (2015) 62–99. https://doi.org/10.1016/j.ijplas.2015.01.005.

[11] J.W. Signorelli, M.A. Bertinetti, P.A. Turner, Predictions of forming limit diagrams using a rate-dependent polycrystal self-consistent plasticity model, Int. J. Plast. 25 (2009) 1–25. https://doi.org/10.1016/j.ijplas.2008.01.005.

[12] L. Cauvin, B. Raghavan, S. Bouvier, X. Wang, F. Meraghni, Multi-scale investigation of highly anisotropic Zinc alloys using crystal plasticity and inverse analysis, Mater. Sci. Eng. A. 729 (2018). https://doi.org/https://doi.org/10.1016/j.msea.2018.05.038.

[13] M. Borodachenkova, W. Wen, F. Barlat, A. Pereira, J. Grácio, Modeling of the mechanical behavior and texture evolution in Zn alloys during reverse shear loading, J. Mater. Process. Technol. 224 (2015) 143–148. https://doi.org/10.1016/j.jmatprotec.2015.04.021.

[14] F. Schlosser, J. Signorelli, M.E. Leonard, A. Roatta, M. Milesi, N. Bozzolo, Influence of the strain path changes on the formability of a zinc sheet, J. Mater. Process. Technol. 271 (2019) 101–110. https://doi.org/10.1016/j.jmatprotec.2019.03.026.

[15] F. Humphreys, M. Hatherly, Recrystallization and Related Annealing Phenomena, 2nd. Ed., Elsevier Ltd., Oxford, 2004.

[16] K. Huang, R.E. Logé, A review on dynamic recrystallization phenomena in metallic materials, Mater. Des. 111 (2016) 548–574. https://doi.org/10.1016/j.matdes.2016.09.012.

[17] J.C. Tan, M.J. Tan, Dynamic continuous recrystallization characteristics in two stage deformation of Mg-3Al-1Zn alloy sheet, Mater. Sci. Eng. A. 339 (2003) 124–132. https://doi.org/10.1016/S0921-5093(02)00096-5.

[18] R. Kaibyshev, Dynamic recrystallization in magnesium alloys, Woodhead Publishing Limited, 2012. https://doi.org/10.1533/9780857093844.1.186.

[19] D. Griffiths, Explaining texture weakening and improved formability in magnesium rare earth alloys, Mater. Sci. Technol. 31 (2015) 10–24. https://doi.org/10.1179/1743284714Y.0000000632.

[20] S.E. Ion, F.J. Humphreys, S.H. White, Dynamic recrystallisation and the development of microstructure during the high temperature deformation of magnesium, Acta Metall. 30 (1982) 1909–1919. https://doi.org/10.1016/0001-6160(82)90031-1.

[21] A. Galiyev, R. Kaibyshev, G. Gottstein, Correlation of plastic deformation and dynamic recrystallization in magnesium alloy ZK60, Acta Mater. 49 (2001) 1199–1207. https://doi.org/10.1016/S1359-6454(01)00020-9.

[22] X. Yang, H. Miura, T. Sakai, Dynamic Evolution of New Grains in Magnesium Alloy AZ31 during Hot Deformation, Mater. Trans. 44 (2003) 197–203. https://doi.org/10.2320/matertrans.44.197.

[23] H. Miura, M. Ito, X. Yang, J.J. Jonas, Mechanisms of grain refinement in Mg-6Al-1Zn alloy during hot deformation, Mater. Sci. Eng. A. 538 (2012) 63–68. https://doi.org/10.1016/j.msea.2012.01.014.

[24] C.D. Barrett, A. Imandoust, A.L. Oppedal, K. Inal, M.A. Tschopp, H. El Kadiri, Effect of grain boundaries on texture formation during dynamic recrystallization of magnesium alloys, Acta Mater. 128 (2017) 270–283. https://doi.org/10.1016/j.actamat.2017.01.063.

[25] L.A. Neumeier, J.S. Risbeck, Influence of Rolling Temperature and Cu content on creep and other properties of Zn-Cu and Zn-Cu-Ti alloys, 1970.

[26] H. Naziri, R. Pearce, Superplasticity in a Zn-0.4%Al alloy, Acta Metall. 22 (1974).

[27] A.S. Malin, M. Hatherly, V. Piegerova, Microstructure and Texture of Rolled C.P.H. Metals, in: R.C. Gifkins (Ed.), 6th Int. Conf. Strength Met. Alloy. (ICSMA 6), Melbourne, Australia, 1982: pp. 523–528.

[28] D. Solas, C.N. Tomé, O. Engler, H.R. Wenk, Deformation and recrystallization of hexagonal metals: Modeling and experimental results for zinc, Acta Mater. 6454 (2001). https://doi.org/10.1016/S1359-6454(01)00261-0.

[29] F. Bachmann, R. Hielscher, H. Schaeben, Grain detection from 2d and 3d EBSD data-Specification of the MTEX algorithm, Ultramicroscopy. 111 (2011) 1720–1733. https://doi.org/10.1016/j.ultramic.2011.08.002.

[30] F. Schlosser, C. Schwindt, V. Fuster, A. Tommasi, J.W. Signorelli, Crystallographic Texture Evolution of a Zinc Sheet Subjected to Different Strain Paths, Metall. Mater. Trans. A Phys. Metall. Mater. Sci. 48 (2017) 2858–2867. https://doi.org/10.1007/s11661-017-4069-y.

[31] X. Chen, W. Jeitschko, M.E. Danebrock, C.B.H. Evers, K. Wagner, Preparation, Properties, and Crystal Structures of Ti3Zn22 and TiZn16, J. Solid State Chem. 118 (1995) 219–226. https://doi.org/10.1006/jssc.1995.1337.

[32] M. Milesi, R.E. Logé, D. Pino Muñoz, Y. Jansen, P.O. Bouchard, Accounting for material parameters scattering in rolled zinc formability, J. Mater. Process. Technol. 245 (2017) 134–148. https://doi.org/10.1016/j.jmatprotec.2017.02.021.

[33] M.H. Yoo, Slip, twinning, and fracture in hexagonal close-packed metals, Metall. Trans. A. 12 (1981) 409–418. https://doi.org/10.1007/BF02648537.

[34] M. Faur, G. Cosmeleaţă, Effects of hot and cold rolling on the microstructure of low alloy Zn-Cu and Zn-Cu-Ti zinc alloy with improved corrosion resistance, UPB Sci. Bull. Ser. B Chem. Mater. Sci. 68 (2006) 67–74.

[35] T.G. Langdon, Twenty-five years of ultrafine-grained materials: Achieving exceptional properties through grain refinement, Acta Mater. 61 (2013) 7035–7059. https://doi.org/10.1016/j.actamat.2013.08.018.

[36] D.A.C. Williams, H. Naziri, R. Pearce, Extended plasticity in commercial-purity zinc, Scr. Metall. 3 (1969) 117–120.

[37] H. Naziri, R. Pearce, The effect of grain size on workhardening superplasticity in Zn-0.4% Al alloy, Scr.

Metall. 3 (1969) 811–814.

[38] A.G. Beer, M.R. Barnett, Microstructural development during hot working of Mg-3Al-1Zn, Metall. Mater. Trans. A Phys. Metall. Mater. Sci. 38 (2007) 1856–1867. https://doi.org/10.1007/s11661-007-9207-5.

[39] É. Martin, J.J. Jonas, Evolution of microstructure and microtexture during the hot deformation of Mg-3% Al, Acta Mater. 58 (2010) 4253–4266. https://doi.org/10.1016/j.actamat.2010.04.017.

[40] G. Zhou, Z. Li, D. Li, Y. Peng, H. Wang, P. Wu, Misorientation development in continuous dynamic recrystallization of AZ31B alloy sheet and polycrystal plasticity simulation, Mater. Sci. Eng. A. 730 (2018) 438–456. https://doi.org/10.1016/j.msea.2018.05.095.

[41] S.I. Wright, M.M. Nowell, D.P. Field, A Review of Strain Analysis Using Electron Backscatter Diffraction, Microsc. Microanal. 17 (2011) 316–329. https://doi.org/10.1017/S1431927611000055.

[42] N. Allain-Bonasso, F. Wagner, S. Berbenni, D.P. Field, A study of the heterogeneity of plastic deformation in IF steel by EBSD, Mater. Sci. Eng. A. 548 (2012) 56–63. https://doi.org/10.1016/j.msea.2012.03.068.

[43] J.A. del Valle, O.A. Ruano, Influence of texture on dynamic recrystallization and deformation mechanisms in rolled or ECAPed AZ31 magnesium alloy, Mater. Sci. Eng. A. 487 (2008) 473–480. https://doi.org/10.1016/j.msea.2007.11.024.

[44] J.J. Gilman, Plastic anisotropy of zinc monocrystals, Trans. Metall. Soc. AIME. 206 (1956) 1326–1336.

[45] R. Parisot, S. Forest, A. Pineau, F. Grillon, X. Demonet, J.-M. Mataigne, Deformation and damage mechanisms of zinc coatings on hot-dip galvanized steel sheets: Part II. Damage modes, Metall. Mater. Trans. A. 35 (2004) 813–823. https://doi.org/10.1007/s11661-004-0008-9.

List of figures

Figure 1. Microstructure and crystallographic texture of the Zn-Cu-Ti sheet in the as-received condition. (a) and (b): band contrast of the EBSD maps taken from the RD-ND and RD-TD sections, respectively. Some large, elongated grains are indicated by arrows and clusters of small, equiaxed grains are bounded in dashed boxes. (c) Secondary electron micrograph revealing the $TiZn_{16}$ phase. (d) Basal and prismatic pole figures recalculated from the EBSD data (X and Y labels correspond to TD and RD, respectively).

Figure 2. Bilinear tensile test (UAT+UAT) of the Zn-Cu-Ti sheet. (a) Sample pre-strained along RD with the major true strain field measured by digital image correlation. Geometry of the second UAT samples are shown in dashed lines. (b) Corresponding flow curves. The prestrain value of the second-step samples is ~0.31.

Figure 3. Band contrast maps and pole figures of the deformed Zn-Cu-Ti samples. (a) and (c): UAT prestrain (ε~0.31). (b) and (d): second UAT loading (ε~0.66). X and Y labels correspond to TD and RD, respectively.

Figure 4. Grain boundaries plotted over orientation maps corresponding to the IPF with respect to the TD. (a) As-received; (b) UAT prestrain (ε~0.31); (c) second UAT loading (ε~0.66). Black lines: HABs (θ>12°); gray lines: LABs (2°<θ≤12°). (d) Detail showing $\{10\bar{1}2\}\langle10\bar{1}\bar{1}\rangle$ twin boundaries in white.

Figure 5. Grain statistics of the Zn-Cu-Ti sheet microstructure for each strain level, subdividing the populations by a size criterion: (a) number density of reconstructed grains; (b) average grain sizes (calculated as equivalent circle diameter); (c) mean aspect ratios. Error bars correspond to the standard deviation of each population.

Figure 6. Map detail illustrating fragmentation of the larger grains (ε~0.31). Gray lines: HABs (θ>12°) of small grains (≤3 μm); black lines: HABs of larger grains (>3 μm); thick red lines: LABs (2<θ≤12°) of subgrains within large grains; thin red lines: inner LABs. Blue: subgrains within large grains; light blue: large grains without subgrains or region of a large grain with an area greater than 50% of the whole grain area (i.e., unfragmented parent grains).

Figure 7. Evolution of the populations of grains and subgrains, and of the fraction of large grains which are not fragmented (number density of small grains is repeated from Fig. 5 for reference).

Figure 8. Misorientation gradients across fragmented grains: (a) and (b) EBSD map details of the first (ε~0.31) and the second (ε~0.66) UAT tests, respectively. (c–e) Changes of misorientation angle over the lines indicated in the maps (solid lines: cumulative or point-to-origin misorientation; dotted lines: point-to-point misorientation).

Figure 9. Grain orientation spread (GOS) maps for the Zn-Cu-Ti sheet under study. (a) As-received; (b) UAT prestrain (ε~0.31); (c) second UAT loading (ε~0.66). HABs (θ>12°) are displayed in black lines. (d) Average GOS values for the subpopulations of grains in each map (error bars correspond to the standard deviation).

Figure 10. Differences in the fragmentation process of the Zn-Cu-Ti sheet according to the mean orientation of the larger grains. Group I: large grains whose *c*-axis have an angular deviation to the ND greater than 45°; group II: large grains with *c*-axis inclined to the ND closely than 45°. The fragmented fraction (a) and the average amount of subgrains per grain (b) are higher for grains of group II.

Figure 11. Distribution of misorientation axes across boundaries (within the group of grains with *c*-axis deviation from the ND <45°) for the conditions indicated. Left and middle columns: LABs within large grains in the angular ranges specified. Right column: HABs of small grains with misorientation angles ranging from 12° to 20°.

Figure 12. Effect of a higher strain rate (5×10^{-1} s^{-1}) on the second UAT test of the Zn-Cu-Ti sheet. (a) Flow curve (the second low-strain rate test is repeated for reference). (b) EBSD map for the high strain-rate test (total strain level ~0.50): grain boundaries plotted over IPF-TD map; black lines: HABs (θ>12°), gray lines: LABs (2°<θ≤12°), white lines: $\{10\bar{1}2\}\langle 10\bar{1}\bar{1}\rangle$ twin boundaries. (c) Comparison of (sub)grain numbers and fragmented fractions of large grains between low (gray dotted lines) and high strain rates (colored solid lines).